A01-16802

AIAA 2001-1008

# FLOW STRUCTURE AND PERFORMANCE OF AXISYMMETRIC SYNTHETIC JETS

Michael O. Müller, Luis P. Bernal,
Paul K. Miska, Peter D. Washabaugh
Department of Aerospace Engineering

Tsung-Kuan Allen Chou, Babak Amir Parviz, Chunbo Zhang, Khalil Najafi
Department of Electrical Engineering
and Computer Science

University of Michigan
Ann Arbor, MI 48109-2140

**39th Aerospace Sciences Meeting & Exhibit**
8-11 January 2001 / Reno, NV

AIAA-2001-1008

# FLOW STRUCTURE AND PERFORMANCE OF AXISYMMETRIC SYNTHETIC JETS

Michael O. Müller*, Luis P. Bernal†, Paul K. Miska¥, Peter D. Washabaugh†,
Tsung-Kuan Allen Chou‡, Babak Amir Parviz‡, Chunbo Zhang‡, Khalil Najafi§

University of Michigan
Ann Arbor, MI 48109-2140

## ABSTRACT

Experimental analysis is presented of the flow structure and performance of axisymmetric synthetic jets. We report direct thrust and Particle Image Velocimetry (PIV) measurements at varying amplitude and frequency for Reynolds numbers in the range 200-2200. It is shown that the jet performance is determined by the flow length, L, defined as the length of fluid ejected during the output stroke of the synthetic jet. Two flow regimes are identified. At small flow lengths L/D < ~3, the thrust is less than the momentum flux ejected during the output stroke, and increases proportional to $L^4$. This reduced thrust is due to re-ingestion of vorticity during the intake stroke. At large flow lengths L/D > ~3, the thrust equals the momentum flux ejected during the output stroke, and is proportional to $L^2$. The entrainment rate of the synthetic jet was measured and found comparable to that of conventional axisymmetric turbulent jets. The mean and time-resolved flow structure in the near field of the synthetic jet varies with flow length. At small flow lengths, vortex rings form close to the orifice and loose some of the vorticity during the input stroke. At large flow lengths, vortex rings with some trailing vorticity form and move away from the orifice thus avoiding re-ingestion of vorticity during the input stroke. The amount of trailing vorticity does not affect the thrust produced by the synthetic jet.

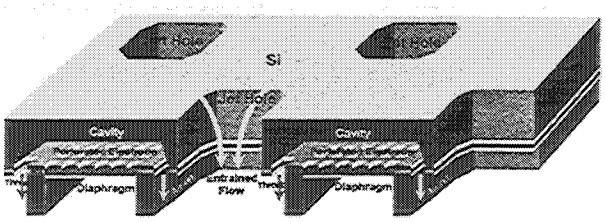


FIGURE 1: Micromachined Ejector Concept.[5]

## INTRODUCTION

The main focus of the present study is to gain a better understanding of the flow structure of synthetic jets and its relation to the thrust and entrainment characteristics of the jets. The research is motivated by an ongoing effort to develop a new technique for propulsion and control of micro airborne platforms (MAPs)[1,2,3,4]. This system (Micromachined Acoustic Ejector, MACE) uses synthetic jets produced by Helmholtz-type acoustic resonators located in an ejector shroud to generate thrust as illustrated in Figure 1.[5] Each resonator consists of a throat, a resonator cavity and an electrostatically driven membrane. The ejector shroud augments the propulsion efficiency of the system. The MACE devices are ideally suited for implementation in MEMS because at the small scales typical of MEMS devices the resonator can be operated at very high frequency thus increasing the Reynolds number and minimizing viscous loses. Using MEMS fabrication techniques, the MACE devices can be integrated into large arrays to produce the necessary thrust for propulsion of MAPs. In addition to a propulsion system for a MAP, other potential applications of this technology include air pumps for cooling applications (IC electronics), fluidic actuators, and flow control of aerodynamic surfaces.

* Graduate Research Assistant, Department of Aerospace Engineering. Member, AIAA.
† Associate Professor, Department of Aerospace Engineering. Senior Member, AIAA.
¥ Undergraduate Research Assistant, Department of Aerospace Engineering.
‡ Graduate Research Assistant, Department of Electrical Engineering and Computer Science.
§ Professor, Department of Electrical Engineering and Computer Science.

Ingård and Labate,[6] in 1950, published a thorough experimental investigation of acoustical streaming phenomena in circular orifices. Their research builds on work by Eckart[7] in 1948 and Lord Raleigh in 1896, who observed "while experimenting with ... brass resonators of pitch *c'*, ... when the corresponding fork, strongly excited, was held to the mouth, a wind of considerable force issued from the nipple at the opposite side. This effect may rise to such intensity as to blow out a candle upon whose wick the stream is directed."[8] One of the first published observations of acoustic streaming is an 1831 publication by Faraday[9], documenting a steady flow resulting from a sound wave propagating through a fluid medium. Synthetic jets are a form of acoustic streaming. In the classification proposed by Ingård and Labate, the flow regime is "region 4: A high sound intensity region in which pulsatory effects are predominant, resulting in the formation of jets and vortex rings. The jet consists of a strong air flow through the orifice, signified by a sudden burst of air. This burst appears symmetrically on both sides of the orifice and is made up of pulses contributed by each cycle of the sound wave."

Smith and Glezer[10] report a comprehensive investigation of 2-D synthetic jets in air. They distinguish between the near and far fields. The flow in the near field is characterized by the formation of vortex pairs. The vortices decelerate and transition to turbulence within 7 slot widths. The trajectory of the vortices scales with the "stroke" length defined as

$$L = \int_{\substack{0 \\ u_e>0}}^{T} u_e \, dt \,, \qquad (1)$$

where $u_e$ is the velocity at the center of the orifice, and T the period of the acoustic oscillation. The use of the "stroke" length is motivated by studies of the formation and evolution of vortex rings[11,12,13] which as noted by Ingård and Labate are an important part of the flow. In the far field Smith and Glezer find a mean flow structure similar to a 2-D turbulent jet, but with slightly different growth rate and center plane velocity decay, which they attribute to reduced static pressure at the orifice.

Muller *et al.*[2,4] describe a reduced order model of synthetic jets driven by an acoustic resonator. The model was developed to predict the performance of the micromachined acoustic ejectors. They note that the flow topology is different for the input stroke and the output stroke of the acoustic cycle, and use the time-averaged downstream momentum flux introduced into the flow field during the output stroke as the primary source of thrust. This momentum flux, however, could be reduced by low static pressure at the orifice as well as downstream momentum re-ingestion into the cavity during the input stroke.

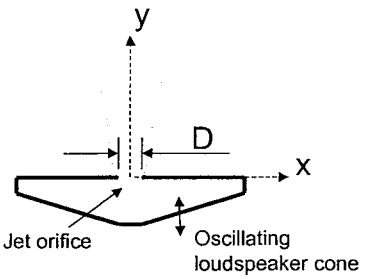


FIGURE 2: Schematic diagram of the synthetic jet set-up, showing general layout and coordinate system: the y-axis is the symmetry axis of the jet.

An equivalent perspective on synthetic jet flows is obtained by considering the dynamics of the vorticity introduced by the acoustic field. During the output stroke, vorticity is introduced into the field forming a vortical structure (vortex pair in 2-D, vortex ring in axisymmetric flow) that propagates away from the orifice. During the input stroke some of the vorticity might be re-ingested back into the acoustic cavity reducing the amount of vorticity in the field. Ultimately it is the impulse associated with the vorticity in the field that accounts for the thrust produced by the device. Gharib *et al.*[14] noted that there is an upper bound for the circulation of vortex rings produced by a piston. For large stroke lengths some vorticity introduced at the orifice is not advected with the main vortex ring. Gharib *et al.* found that the vortex ring attains maximum circulation for a stroke-to-diameter ratio of about 4.

Another important aspect of the MACE propulsion concept is thrust amplification by the ejector shroud. This process relies on entrainment of ambient fluid by the synthetic jet. Smith and Glezer[9] measured the entrainment of 2-D synthetic jets and noted reduced entrainment compared to a conventional 2-D jet.

In this investigation we consider the flow characteristics of an axisymmetric synthetic jet.

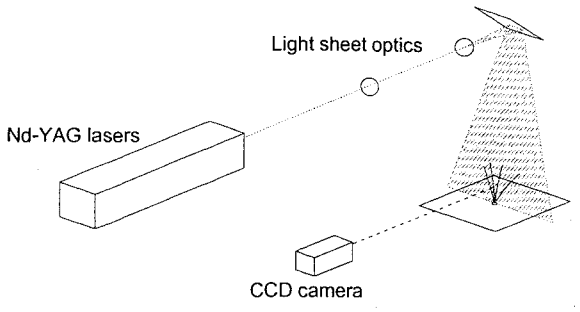


FIGURE 3: Schematic diagram of the synthetic jet set-up for the PIV measurements.

The flow geometry and axes are shown in Figure 2. In addition to the fluid properties $\rho$ and $\mu$, the scaling parameters are the orifice diameter, D, and the frequency, f, and amplitude of the oscillatory flow at the orifice. Following Muller *et al.*[2,4] the amplitude is characterized in terms of the flow length, L, defined by equation (1) and the total circulation introduced during the output stroke,

$$\Gamma_o = \frac{1}{2}\int_{\substack{0\\ u_e>0}}^{T} u_e^2\, dt \quad \text{..... (2)}$$

As noted by Smith and Glezer[10] the characteristic speed $U_o = \Gamma_o/L$ is useful scaling velocity for synthetic jet flows. The performance of the synthetic jet is characterized in terms of the thrust, $T_h$, and the entrainment rate defined as the rate of change of the mass flux with downstream distance, $\dot{m}_y$. Mueller *et al.*[2] show that the thrust of the synthetic jet is related to the circulation by the equation,

$$T_h = 2\rho\,\Gamma_o\, f\, A_{je} \quad \text{..... (3)}$$

where $A_{je}$ is the effective cross section area of the jet orifice. The relevant non-dimensional parameters are the stroke to diameter ratio, L/D; the Reynolds number, $Re = \frac{\rho f D^2}{\mu}$; the thrust coefficeint, $C_T = \frac{T_h}{\rho D^4 f^2}$; and the mass entrainment coefficient, $C_m = \frac{\dot{m}_y}{\rho D^2 f}$. Thus in the present investigation we seek to determine experimentaly $C_T(L/D,Re)$, $C_m(L/D,Re)$ and their relation to the vortical flow structure of a synthetic axisymmetric jet.

## FLOW APPARATUS AND INSTRUMENTATION

Figure 2 shows schematically the synthetic jet apparatus. It consists of an oscillating loudspeaker cone covered by a flat plate containing the circular jet orifice. The loudspeaker diameter is 20 *cm* and the orifice diameter is exactly 1.27 *cm*. An audio power amplifier drives the loudspeaker cone at the desired frequency (pure tone). An optical position probe located near the outer edge of the loudspeaker cone monitors the amplitude of the loudspeaker motion.

The thrust and velocity field produced by the synthetic jet were measured. Direct thrust measurements were conducted by mounting the entire synthetic jet apparatus on an analytic balance with a resolution of 0.5 *mN*. The velocity field was measured using a Particle Image Velocimetry (PIV) system shown schematically in Figure 3. The flow was seeded with nebulized smoke oil, illuminated by two Nd-YAG lasers, and imaged with a high-resolution two-frame CCD digital camera. Each PIV image consists of two particle images obtained with elapse time in the range 5-30 $\mu$s. An enclosure above the orifice (not shown in Figure 3) shielded the synthetic jet from air currents in the room.

The field of view of the PIV system was 7 *cm* wide (x-direction) by 6 *cm* tall (y-direction). Each image was 1024 x 896 *pixels*, which gives a resolution of 147 *pixel/cm*. The PIV images were processed using a cross correlation algorithm. A 64 *pixels* (0.44 *cm*) square interrogation window was used

**TABLE 1: Tests Conditions Summary**

| f (Hz) | L/D | Re | Sym. | f (Hz) | L/D | Re | Sym. |
|---|---|---|---|---|---|---|---|
| 20 | 6.3 | 215 | ◆ | 160 | 2.3 | 1720 | ◆ |
| 30 | 4.8 | 323 | ◆ | 170 | 2.2 | 1828 | ◆ |
| 40 | 4.3 | 430 | ◆ | 180 | 2.1 | 1935 | ◆ |
| 50 | 3.9 | 538 | ◆ | 190 | 2.2 | 2043 | ◆ |
| 60 | 3.6 | 645 | ◆ | 200 | 2.1 | 2151 | ◆ |
| 70 | 2.9 | 753 | ◆ | 50 | 2.2 | 538 | O |
| 80 | 3.1 | 860 | ◆ | 50 | 2.5 | " | O |
| 90 | 2.8 | 968 | ◆ | 50 | 3.0 | " | O |
| 100 | 2.8 | 1075 | ◆ | 50 | 3.9 | " | O |
| 110 | 2.8 | 1183 | ◆ | 50 | 5.6 | " | O |
| 120 | 2.7 | 1290 | ◆ | 150 | 1.8 | 1613 | ● |
| 130 | 2.7 | 1398 | ◆ | 150 | 2.4 | " | ● |
| 140 | 2.3 | 1505 | ◆ | 150 | 3.1 | " | ● |
| 150 | 2.6 | 1613 | ◆ | | | | |

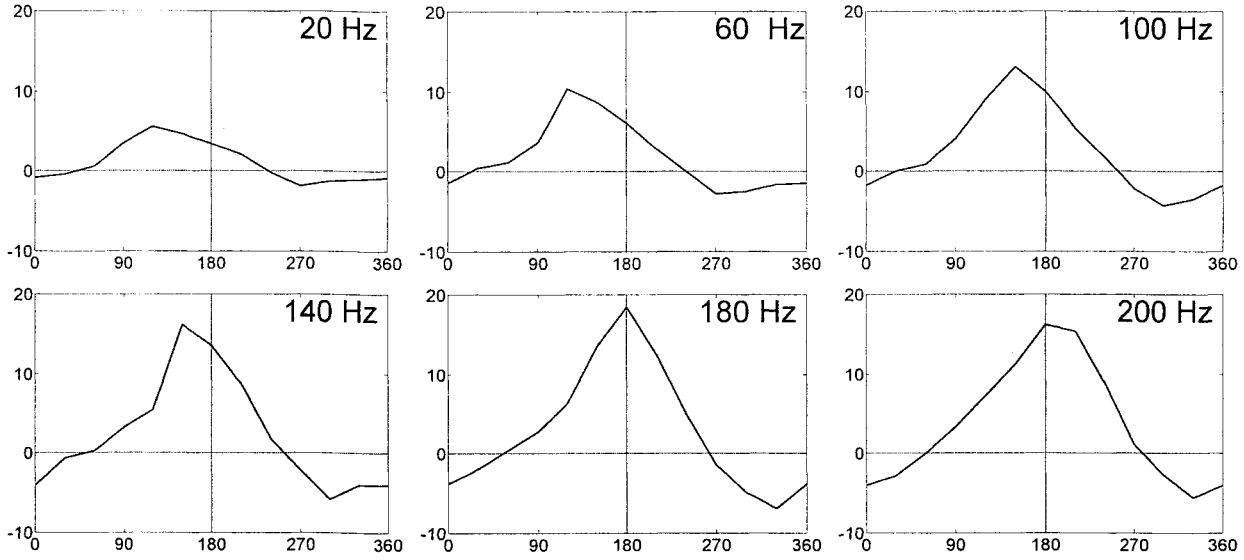


FIGURE 3: Flow velocity measured on the axis of symmetry close to the orifice (x/D = 0; y/D = 0.25) at the frequency indicated on each plot. The vertical axis is the velocity in *m/s* and the horizontal axis is the phase angle relative to the phase of the loudspeaker cone velocity. Phase less than 180° corresponds to the upstroke of the loudspeaker cone.

to measure the velocity vector on a square grid with an overlap factor of 8 (i.e. the grid spacing was 8 pixels (0.055 cm)). Typically each PIV image was processed to give the velocity field on a rectangular region with 128 x 112 points. For each flow condition listed in Table 1 PIV images were taken at 30 degrees phase intervals through the acoustic cycle. Nine realizations were recorded for each flow condition and at each phase. All the results presented here are based on phase averaged PIV data. For each case images at the same phase were individually processed and the median of the nine realizations used. The total number of processed images is 1,944, and the total number of velocity vectors is a staggering 28 million!

A total of 27 cases were tested at the conditions shown in Table 1. Two different types of tests were conducted. In the first series of tests the amplitude of the loudspeaker motion, as determined from the optical position probe, was kept constant and the frequency was varied in the range 20 – 200 *Hz*. These tests attempted to identify resonance phenomena of the acoustic cavity. In the second series of tests the frequency was kept constant and the amplitude of the loudspeaker motion was changed. Two frequencies 50 *Hz* and 150 *Hz* were used. The latter is close to the expected acoustic cavity resonance, and the first is at a frequency at which the diaphragm could be driven to very large amplitudes.

Table 1 also gives the non-dimensional amplitude L/D and the Reynolds number for each test case. The flow length L was determined using equation (1). It should be noted that although in the first series of tests the amplitude of loudspeaker motion was kept constant, the value of L/D decreased as the frequency was increased. This is attributed to flow leakage through the loudspeaker cone. Also the tests at 150 *Hz* and varying amplitude could not be conducted at L/D > 3.1 because of limitations of the power amplifier.

## RESULTS

### Orifice Flow Characterization

Figure 3 shows the velocity at the orifice during the acoustic cycle at several frequencies (20, 60, 100, 140, 180 and 200 *Hz*). These data are the velocity measured with the PIV system on the axis of symmetry at y/D = 0.25, the closest distance at which the flow velocity could be measured reliably. In Figure 3 the horizontal axes are the phase relative to the phase of the loudspeaker cone velocity. As the frequency increases the phase of

the velocity trace varies. At low frequency the maximum orifice velocity lags the loudspeaker velocity by approximately 10°. At high frequency (200 Hz) the phase delay is more than 90°. The phase lag at 20 Hz is attributed to the finite distance from the measurement point to the exit plane of the jet. The larger phase lag at higher frequencies is a manifestation of acoustic resonance in the loudspeaker cavity. Ideally at resonance the phase lag should be 90°. The theoretical prediction for the resonant frequency is 180 *Hz*.[2] This value is consistent with the PIV velocity traces shown in Figure 3.

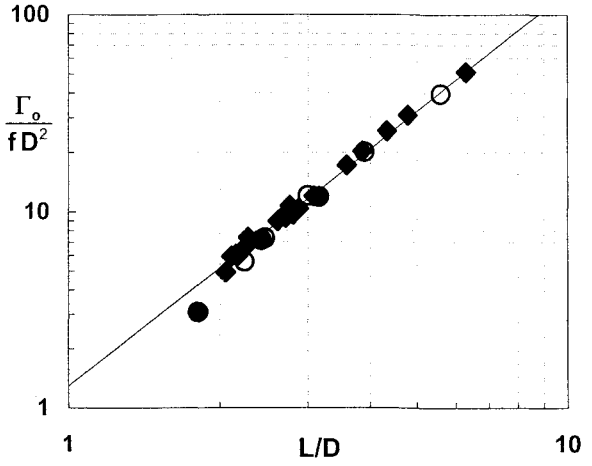


Figure 4: Plot of the measured circulation as a function of the flow length. For key to the symbols see Table 1. Solid line, least squares fit to the data.

For all test cases listed in Table 1 the orifice velocity as shown in Figure 3 were used to calculate the flow length, L, and circulation, $\Gamma_o$, using equations (1) and (2), respectively. The results for the flow length are listed in Table 1. The circulation results are plotted in Figure 4 where the non-dimensional circulation $\Gamma/D^2 f$ is plotted as a function of the non-dimensional flow length L/D. These results show that the circulation increases proportional to $(L/D)^2$. A least square fit to the data gives,

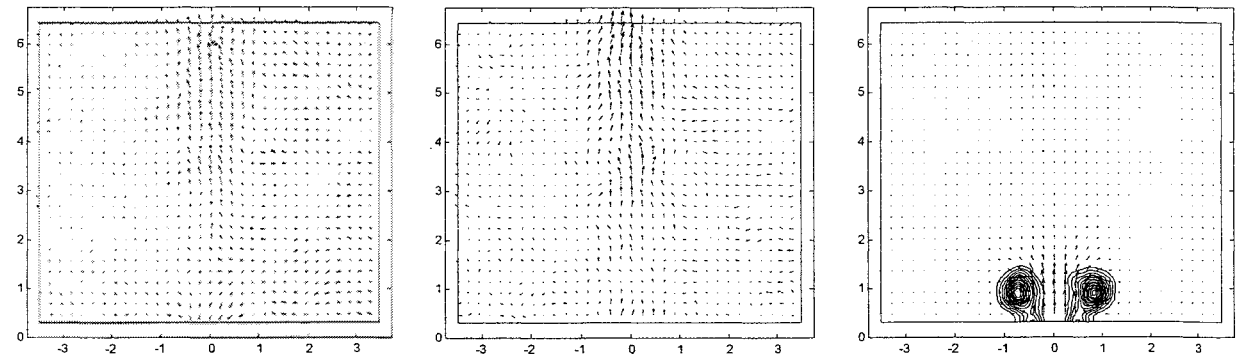

Phase: 0° 60° 120°

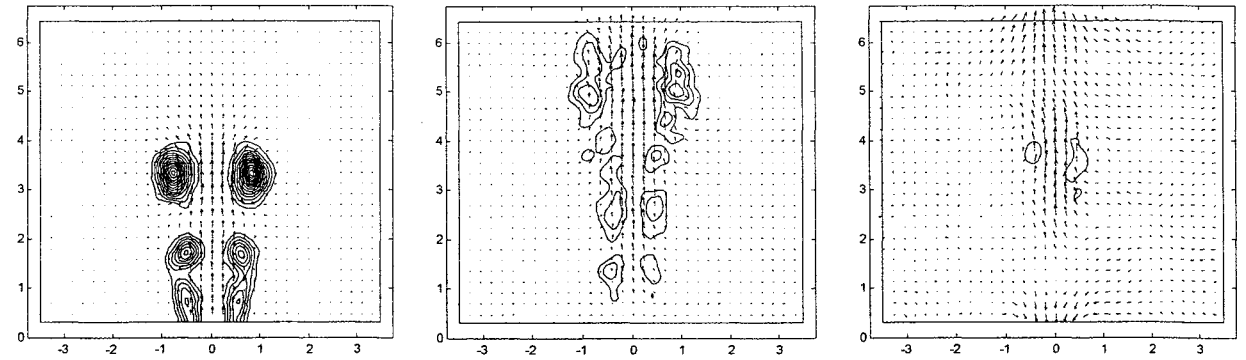

Phase: 180° 240° 300°

FIGURE 5: Sequence of PIV images showing flow structure for f = 20 Hz, L/D = 6.3. Phase 0° corresponds to the loudspeaker cone at bottom dead center; Phase 180° corresponds to top dead center. Vorticity contours start at $\omega/f = \pm 15$ and increment by 10. Horizontal and vertical scales are in *cm*.

$$\frac{\Gamma}{D^2 f} = 1.30\left(\frac{L}{D}\right)^2 \quad \text{..... (4)}$$

It follows that the characteristic velocity of the orifice flow $U_o = \frac{\Gamma}{L}$ is given by the correlation,

$$\frac{U_o}{Df} = \frac{\Gamma}{LDf} = 1.30\frac{L}{D} \quad \text{..... (5)}$$

## Time Resolved Flow Structure

As indicated earlier PIV data were obtained for all cases listed in Table 1. A typical data set consisting of the ensemble average of the velocity and vorticity fields at f = 20 *Hz* and L/D = 6.3 is shown in Figure 5. The flow field at different phases in the acoustic cycle is shown as indicated. These data show a flow topology similar to that described by Ingård and Labate and Smith and Glezer. This particular sequence is at a large value of L/D. In this case the vortical structure formed during the output stroke consists of a concentrated vortex ring followed by a column of vorticity. As the flow evolves the vorticity moves away from the orifice. The data in Figure 5 also show that during the input stroke (when the orifice velocity is negative; phase 300° and 0°) there is no vorticity ingested into the resonator cavity.

The flow topology for f = 200 Hz and L/D = 2.1 is shown in Figure 6. As in the previous case a vortex ring is formed during the output stroke. In this case a column of vorticity does not trail the vortex ring. The vortex ring forms very close to the output orifice and moves at a relatively lower speed. As a result the vortex ring is very close to the orifice when the input stroke begins suggesting that there is significant re-ingestion of vorticity into the loudspeaker cavity (phase 300° and 0°).

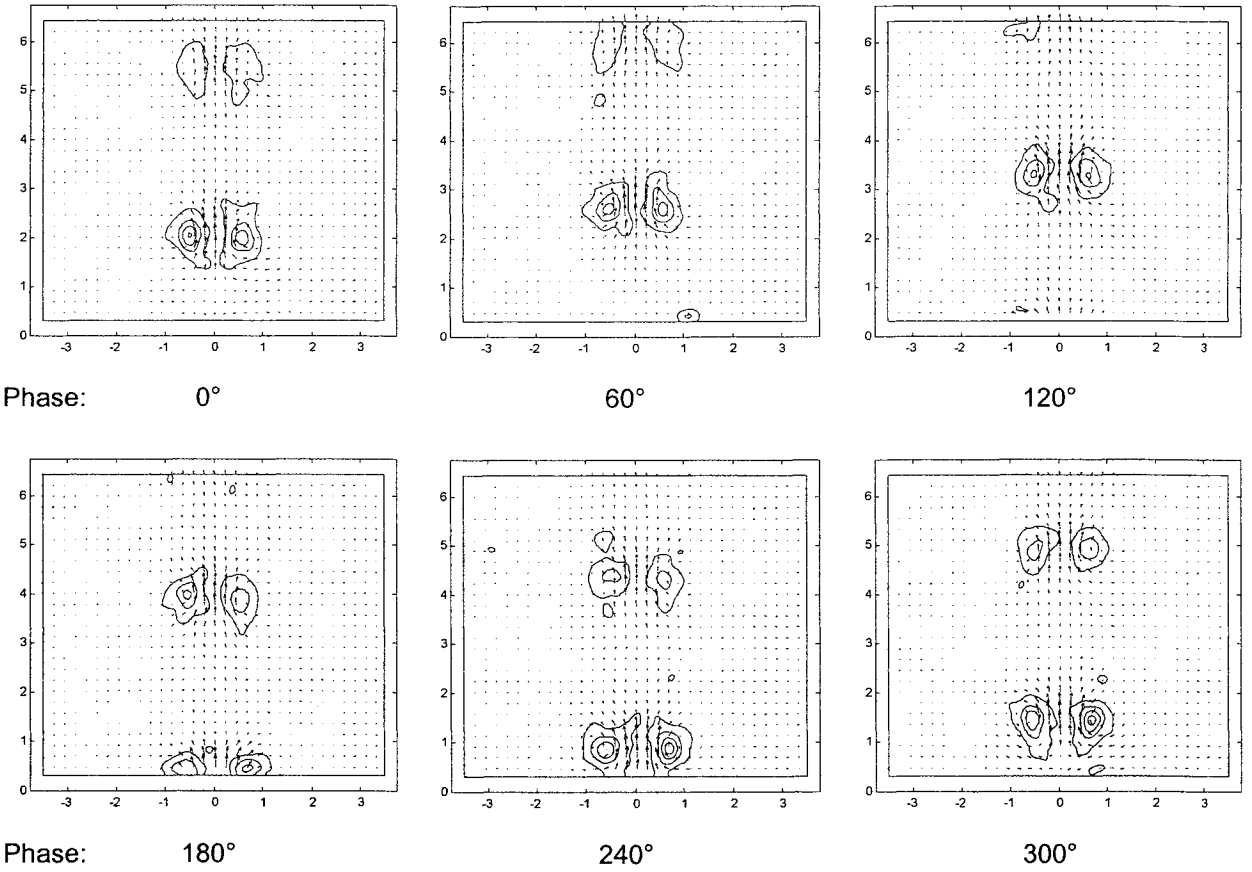


FIGURE 6: Sequence of PIV images showing flow structure for f = 200 Hz, L/D = 2.1. Phase 0° corresponds to the loudspeaker cone at bottom dead center; Phase 180° corresponds to top dead center. Vorticity contours start at $\omega/f = \pm 5$ and increment by 10. Horizontal and vertical scales are in *cm*.

## Mean Flow Structure

The mean flow is calculated by averaging the individual phase PIV images over an entire cycle. Figure 7 shows the cycle averaged velocity plot, with vorticity contours overlaid. The data are for f = 50, L/D = 3.0. One striking feature of the mean flow common to all cases investigated is that the mean flow velocity on the axis of symmetry is always positive. A relatively thin shear layer bounds this region of positive velocity. The shear layer evolution with downstream distance is fairly slow. Figure 8 shows the streamlines computed for the flow in Figure 7. The streamlines clearly document the entrainment pattern of the synthetic jet. The streamline pattern is not symmetric due to a small but pervasive cross flow (somewhat exaggerated by this depiction). The cross flow was observed in all cases investigated. However, as will be shown below, the cross flow does not significantly influence the performance of the synthetic jet. The entrainment pattern of the synthetic jet shows several interesting features. Near the orifice, for y/D < 2, the streamlines approach the jet normal to the y-axis, deflect upstream at the shear layer, and turn downstream as they enter the high speed region near the axis. Farther downstream the streamlines do not show this upstream deflection. The reverse flow region near the orifice is a manifestation of strong suction during the input stroke.

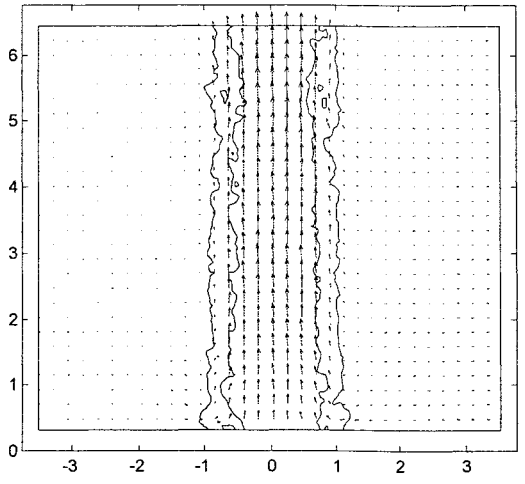


FIGURE 7: Velocity vectors and vorticity contours for the mean jet flow, showing jet growth. (50 Hz, L/D = 3.0 shown). Horizontal and vertical scales are in *cm*. Single vorticity contour shown with $\omega/f = \pm 5$.

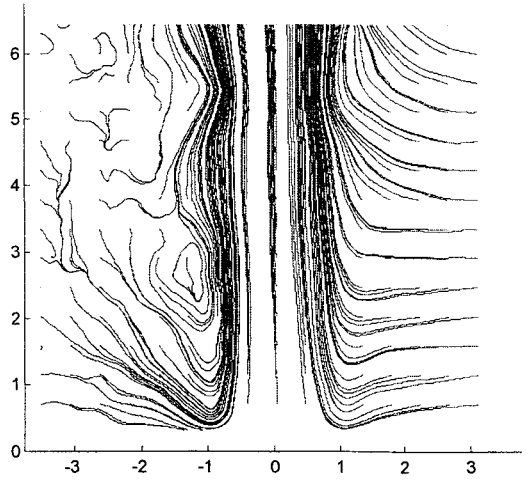


FIGURE 8: Streamlines of synthetic jet over full period, showing fluid entrainment. (20 Hz, L/D = 6.3 shown). Horizontal and vertical scales are in cm.

Figures 9 to 11 quantitatively describe the mean

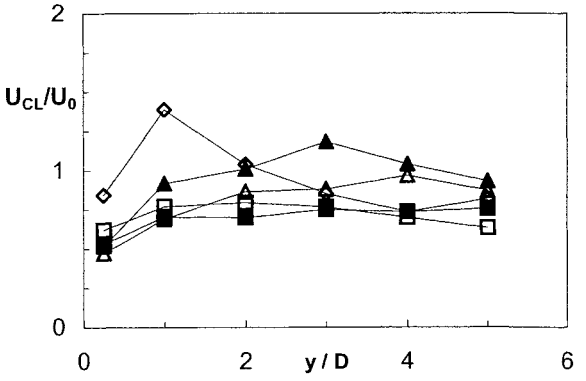


Figure 9: Centerline velocity evolution for f =50. For key to the symbols see Figure 10.

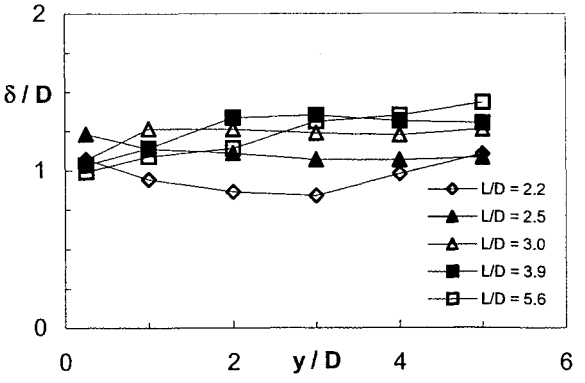


FIGURE 10: Synthetic jet growth rate

flow at 50 Hz. Although all the data reported here was obtained in the near field of the jet, it is convenient to describe the flow in terms of the centerline velocity and half-velocity width defined as the diameter of the jet were the downstream velocity equals half the centerline velocity. Figure 9 shows the evolution of the centerline velocity along the y-axis. The centerline velocity is normalized by the synthetic jet characteristic velocity $U_o = \Gamma_o/L$. The centerline velocity first increases close to the orifice, followed by a decrease. The location of the maximum varies with L/D. At L/D = 2.2, the maximum occurs at y/D = 1. At L/D of 2.5 and 3.0, the maximum occurs at y/D = 3 and 4. Finally, for L/D of 3.9 and 5.6, the y/D peak decreases to 3 and 2, respectively.

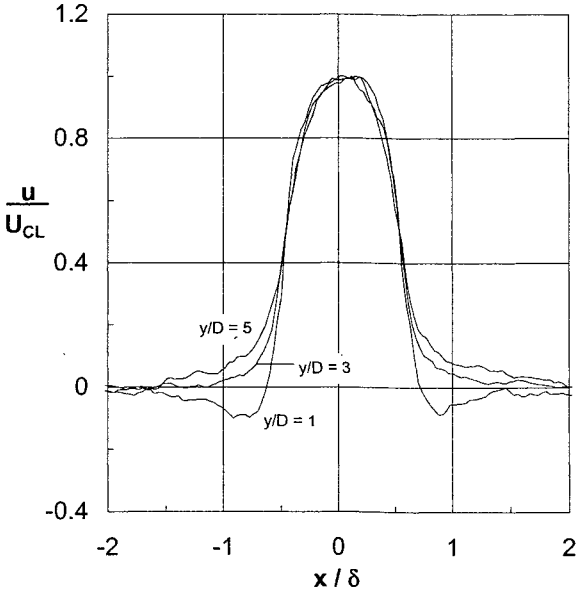


FIGURE 11: Mean velocity profiles for varying y/D.

Figure 10 shows the evolution of the half-velocity jet width, $\delta$, with downstream distance, y. Again, different behavior is observed for varying L/D: at low L/D (L/D = 2.2 and 2.5), the jet width has a local minimum near the exit. At larger L/D values, the jet width increases monotonically with increasing downstream distance.

Plotted in figure 11 are y-velocity profiles at y/D = 1, 3, and 5. The y-velocity is normalized with the centerline velocity, $U_{CL}$, and the horizontal distance x is normalized with $\delta$. There is good collapse of the data in the center region of the jet

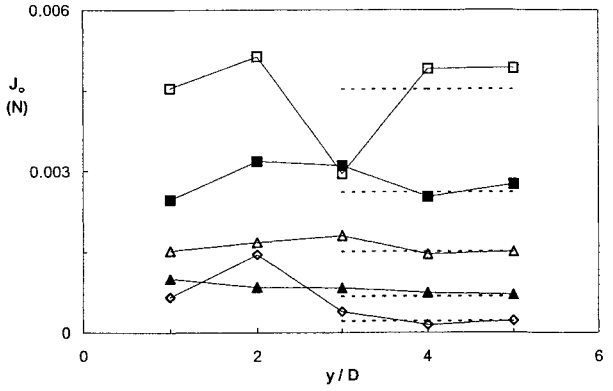


Figure 12: Momentum flux, $J_o$, as a function of y/D for f = 50 Hz. Symbols: momentum flux evaluated on planes normal to the axis. Broken line: momentum flux evaluated using the larger possible control volume. For key to the symbols see Figure 10.

for all values of y/D. The structure of the shear layer, however, varies with y/D. At small values of y/D (y/D = 1) there is a region of negative velocity at the outer edges of the shear layer. At y/D = 3, the velocity is positive across the entire plane. This region of transition, from a mean negative velocity along the outer edge of the shear layer to a mean positive velocity, is also evident in streamline plots like the one shown in Figure 8. Based on the streamline plots the region of negative downstream velocity at the outer edge of the shear lager extends to y/D ~2.

The PIV data can be used to determine the performance of the synthetic jet in terms of the thrust produced and the mass flow entrainment. To determine the thrust and characterize the accuracy of the results the mean momentum flux

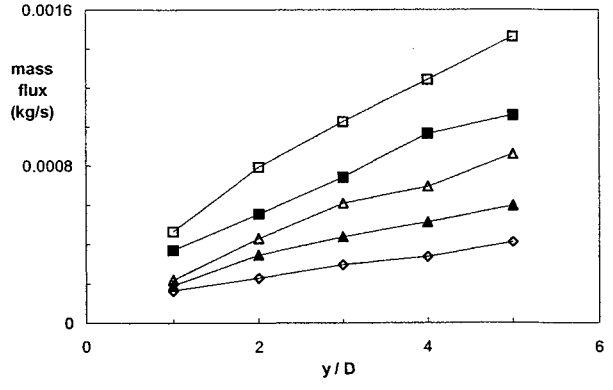


Figure 13: Mass flux on cross section planes normal to the y-axis as a function of y/D for f = 50 Hz. For key to the symbols see Figure 10.

was evaluated using several control volumes. First shown in Figure 12 is the momentum flux evaluated on planes normal to the y-axis as a function of y. Also shown in this figure as horizontal dashed lines is the momentum flux evaluated on a closed control volume bounded by the synthetic jet orifice plate and the largest possible cylindrical surface around the jet (x/D = ±2.75, y/D = 5). The data show that downstream of y/D = 4 the momentum flux is substantially equal to value calculated with the closed control volume; the deviation at lower values of y/D are indicative of changes of the static pressure expected near the orifice. This good agreement suggests that the effect of the cross current mentioned earlier is small, and does not influence the momentum flux calculation. Also it validates the use of mean momentum flux and mass flux calculations to characterize the synthetic jet thrust and entrainment performance.

Figure 13 shows the mean mass flux on planes normal to the flow axis. The results show an approximate linear increase of mass flux with downstream distance. The slope of the curve is the entrainment rate. These results show an increase of the entrainment rate with flow length.

## Synthetic Jet Performance

The thrust produced by the synthetic can be calculated from the PIV measurements by evaluating the momentum flux on a large control volume as described above. However, this method assumes a constant static pressure on the control volume. Thus, the control volume must be at a large enough distance from the orifice.

To validate the PIV results, the thrust was measured directly using an analytic balance. As noted earlier the measurement resolution is 0.5 *mN*. These tests were conducted at nominally the same flow conditions as the PIV measurements based on the output of the optical position probe. Figure 14 is a comparison of the direct thrust measurements and the PIV calculated results. The error bars on the PIV calculated results are an indication of the expected uncertainty based on evaluation of the momentum flux on several, successively smaller, control volumes. The agreement is excellent at low frequency up to about 130 *Hz*. The agreement is not as good at higher frequencies due to limitations of the optical position probe, which did not provide reliable data at high frequencies.

The data in Figure 14 show an increase in thrust with frequency (despite a decreasing L/D), and a

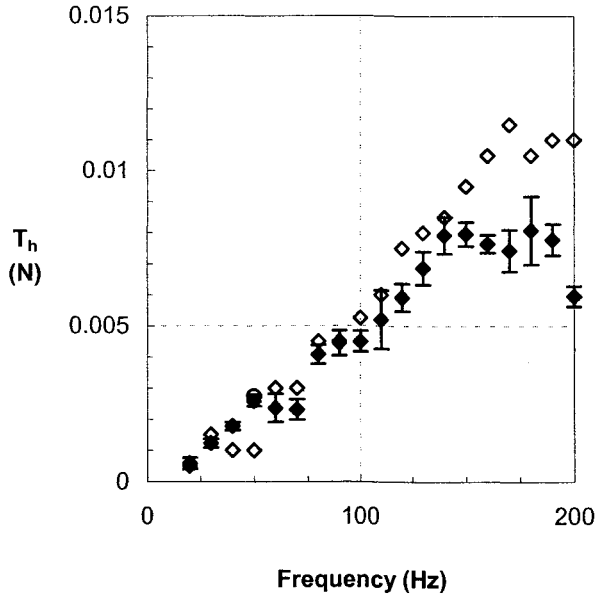


Figure 14: Comparison of the direct thrust measurement results and the PIV calculated thrust showing excellent agreement. Solid symbols PIV data, open circle, PIV data, Open diamond direct thrust measurements.

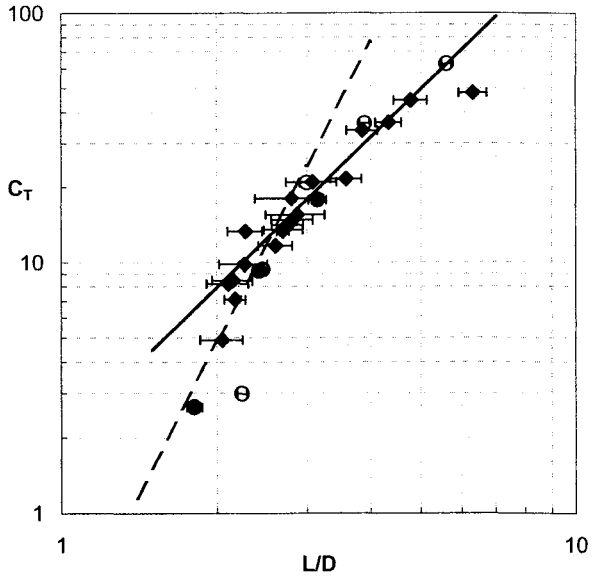


FIGURE 15: $C_T = T / \rho D^4 f^2$ plotted against L/D. Dashed line indicates $(L/D)^4$ correlation for small L/D. Solid line equation (6). Symbols are as listed in table 1.

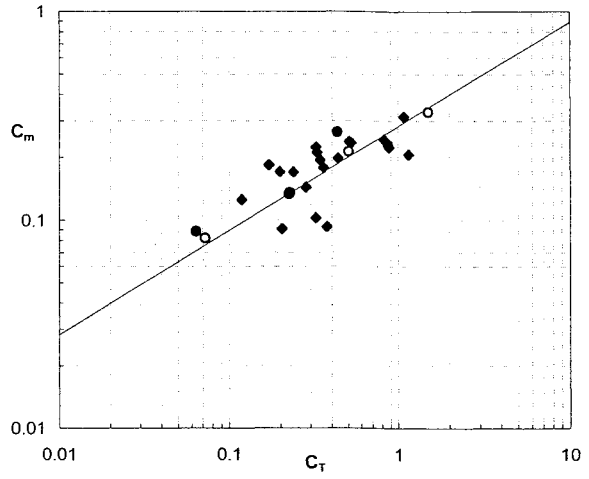


FIGURE 16: $C_m$ as a function of $C_T$. Conventional jet result given by equation (7)[15]. Symbols are as listed in Table 1.

roll-off in performance at frequencies greater than 150-180 Hz. This result is consistent with the acoustic resonance discussed by Muller *et al*[2]. The maximum thrust is at 150-180 *Hz*, the calculated resonant frequency of the acoustic cavity. Thus the thrust measurements and the orifice exit velocity phase results are consistent with the theoretical prediction of the resonant frequency of the acoustic cavity.

The thrust performance of the synthetic jet is shown in Figure 15 in term of the thrust coefficient as function of L/D. The error bars in this figure are based on the uncertainty of the flow length, L. Only PIV results are shown in this figure since it is not possible to determine the flow length for the direct thrust measurement tests. Also shown in the figure is the trend line derived from equation (3) assuming that the effective cross section area of the orifice equals the geometrical area, which gives using equation (5),

$$C_T = \frac{T_h}{\rho D^4 f^2} = \frac{\pi}{2}\frac{\Gamma_o}{D^2 f} = 2.04\left(\frac{L}{D}\right)^2 . \quad \text{..... (6)}$$

Equation (6) is shown as a solid line in Figure 15. The data for L/D < ~3 departs significantly from this trend line. In this region the thrust coefficient is proportional to $(L/D)^4$. The dashed line in the figure identifies this trend

$$C_T = 0.3\left(\frac{L}{D}\right)^4 . \quad \text{..... (7)}$$

The two flow regimes identified in the thrust measurements are associated with the flow changes identified in the time resolved flow structure. At small values of L/D there is re-ingestion of vorticity during the intake stroke of the synthetic jet as a result not all the vorticity and consequently the positive momentum injected during the output stroke is advected away from the orifice. Clearly if the flow length is very small (the linear acoustic regime) all the vorticity is re-ingested into the acoustic cavity. As the flow length increase the amount of vorticity re-ingested is reduced which gives the fast increase of thrust coefficient with L/D. For L/D > ~3 all vorticity remains in the field and the thrust is given by equation (3).

The PIV data were also used to determine the entrainment of the synthetic jet. The rate of change with downstream distance (y) of the mass flux was measured using results similar to those shown in Figure 13 and the mass flow coefficient calculated. The mass flow coefficient is plotted in Figure 16 as a function of thrust coefficient. Also plotted in the figure is the result for a conventional axisymmetric jet[15] given by the relation

$$C_m = \frac{\dot{m}_y}{\rho D^2 f} = 0.282\, C_T^{1/2} . \quad \text{..... (8)}$$

Although there is some data scatter, these measurements indicate that the axisymmetric synthetic jet entrainment is comparable to a conventional jet. This behavior is different than for a 2-D synthetic jet where Smith and Glezer[10] found reduced entrainment compared to a conventional 2-D jet.

## CONCLUDING REMARKS

The flow structure and performance of an axisymmetric synthetic jet has been documented by direct thrust measurements and PIV velocity measurements. The synthetic jet flow field is dominated by the dynamics of the vortical structures formed during the output stroke of the acoustic oscillation. It is found that the flow length is a useful reference length scale that characterizes the amplitude of the acoustic oscillation at jet orifice. Two distinct regimes of operation have been identified. For L/D < ~3 some of the vorticity introduced during the output stroke is re-ingested during the input stroke. In this regime the thrust coefficient is proportional to $(L/D)^4$. In this case the vortex rings form close to

the orifice and lose some vorticity as the input stroke begins. The mean flow is characterized by a neck down of the jet width, and a larger maximum value of the centerline velocity. For L/D > ~3 there is no re-ingestion of vorticity during the input stroke and the synthetic jet thrust equals the positive momentum flux at the orifice. In this regime the thrust coefficient is proportional to $(L/D)^2$. The vortex rings form and move away from the orifice before the input stroke begins, which prevents re-ingestion of vorticity. Significant amounts of trailing vorticity are found for larger values of L/D, although this vorticity does not influence the thrust coefficient scaling. The mean flow in this case is characterized by a moderate increase of the half velocity width with downstream distance, and more gradual evolution of the centerline velocity.

The mass entrainment rate of the axisymmetric synthetic jet is comparable to the mass entrainment rate of conventional axisymmetric jets. This is found for both flow regimes. Another interesting feature common to both flow regimes is the reverse flow region (negative flow velocity) found at the outer edge of the shear layer. This reverse flow region is found only in the very near field of the jet (up to 2 diameters downstream). The maximum negative mean velocity in this region is of the order of 10% of the centerline speed.

The results obtained at varying frequency support the acoustic resonance mechanism proposed by Muller *et al.*[2]. There are two main consequences of the acoustic resonance: there is a rapid increase of the thrust produced by the synthetic jet with increasing frequency even though the flow length decreases in the present tests; and the phase of the orifice flow velocity changes as the frequency approaches the resonant frequency.

Finally we note the many similarities between synthetic jet flows and vortex ring formation flows. These similarities have not escaped other authors[6,10]. There are several useful concepts used here to describe the synthetic jet flow structure, like the flow length, L, the circulation, $\Gamma_o$, and the characteristic velocity $U_o$, that are borrowed from studies of vortex ring formation. However, there are also important differences between these flows. In particular the flow regimes identified in this study are unique to the synthetic jet flow since re-ingestion of vorticity cannot occur in vortex ring formation flows.

## ACKNOWLEDGEMENT

This research was supported by DARPA under contract number N00019-98-K-0111.

## REFERENCES

[1] PARVIZ, B. A., BERNAL L. P., AND NAJAFI, K. 1999 A Micromachined Helmholtz Resonator for Generation of Microjet Flows. 1999 Presented at the *10th international conference on solid-state sensors and actuators (Transducers, '99), June 7-10, 1999, Sendei, Japan.* 1788-1791.

[2] MÜLLER, M. O., BERNAL, L. P., MORAN, R. P., WASHABAUGH, P. D., PARVIZ, B. A. AND NAJAFI, K. 2000 Micromachined Acoustic Resonators for Microjet Propulsion. *AIAA paper 2000-0547.*

[3] MORAN, R.P., WASHABAUGH, P.D., MÜLLER, M.O., BERNAL, L.P., PARVIZ, B.A. AND NAJAFI, K. 2000 Numerical Simulation of Micromachined Acoustic Resonators. *AIAA paper 2000-0546.*

[4] MÜLLER, M.O., BERNAL, L.P., MORAN, R.P., WASHABAUGH, P.D., PARVIZ, B.A., CHOU, T.-K.A., ZHANG, C., AND NAJAFI, K. 2000 Thrust Performance of Micromachined Synthetic Jets. *AIAA paper 2000-2404.*

[5] CHOU, T.-K.A., NAJAFI, K., MÜLLER, M.O., BERNAL, L.P., AND WASHABAUGH, P.D. 2001 High-density micromachined acoustic ejector array for micro propulsion. 2001 To be presented at the *12th international conference on solid-state sensors and actuators (Transducers, '01), Munich, Germany.*

[6] INGÅRD, U. AND LABATE S. 1950 Acoustic Circulation Effects and the Nonlinear Impedance of Orifices. *The Journal of the Acoustical Society of America.* **22,** 211-218.

[7] ECKART, C. 1948 Vortices and Streams Caused by Sound Waves. *Physical Review.* **73,** 68-76.

[8] LORD RALEIGH. 1896 *Theory of Sound, Vol.* 2. p. 217. Macmillan.

[9] FARADAY, M. 1831 *Phil. Transactions.* **Part II,** 299.

[10] SMITH, B. L. AND GLEZER, A. 1998 The formation and Evolution of Synthetic Jets. *Physics of Fluids.* **10,** 2281-2297.

[11] DIDDEN, N. 1979 On the formation of vortex rings: rolling-up and production of circulation. *Z. Angew. Math. Physi.* **30,** 101.

[12] Glezer, A. 1988 The formation of vortex rings. *Phys. Fluids* **31**, 3532

[13] SHARIFF, K. AND LEONARD A. 1992 Vortex Rings. *Annu. Rev. Fluid Mech.* **24**, 235-79.

[14] GHARIB, M., RAMBOD, E. AND SHARIFF, K. 1998 A universal time scale for vortex ring formation. *Journal of Fluid Mechanics.* **360**, 121-140.

[15] RICOU, F.P. AND SPALDING, D.B. 1961 Measurements of entrainment by axisymmetrical turbulent jets. *Journal of Fluid Mechanics.* **11**, 21-31.